

ANALYSIS OF EQUATORIAL F-REGION VERTICAL NEUTRAL WINDS FROM BRAZIL
FPI OBSERVATIONS

by

JOSE DE LA GARZA

Presented to the Faculty of the Graduate School of
The University of Texas at Arlington in Partial Fulfillment
of the Requirements
for the Degree of

MASTER OF SCIENCE IN PHYSICS

THE UNIVERSITY OF TEXAS AT ARLINGTON

AUGUST 2015



Copyright © by Jose De La Garza 2015

All Rights Reserved

Acknowledgements

First of all, I would like to thank my advisor, Yue Deng, for her patience in keeping me as her graduate student while supporting and guiding me all the way along my research. Also, I must acknowledge Cheng Sheng for helping me whenever I had questions about data analysis. Many thanks to Dr. Mingwu Jin and Dr. Sangwook Park for taking the time to serve in my committee. Also I need to thank our collaborator Dr. Jonathan Makela for making this research possible by providing all the equipment needed to obtain the data, and for his technical guidance on handling the data. Finally, I would like to thank my wife for her unconditional love and support that she has given me throughout my academic journey.

June 15, 2015

Abstract

ANALYSIS OF EQUATORIAL F-REGION VERTICAL NEUTRAL WINDS FROM BRAZIL FPI OBSERVATIONS

Jose De La Garza, M.S.

The University of Texas at Arlington, 2015

Supervising Professor: Yue Deng

Understanding the neutral dynamics of our upper atmosphere is an essential component of space weather prediction. In order to come up with better climatological models that describe upper atmospheric variations, an accurate description of vertical neutral winds is needed. Hence, observations of thermospheric winds must be continually made in order to fulfill this need.

Vertical winds are generally smaller than horizontal winds, but even small vertical winds can have a significant effect on the ionosphere and thermosphere because of the large vertical density gradients that exist throughout the atmosphere. Recent observation deployments of Fabry-Perot Interferometers (FPIs) in Brazil have allowed substantial progress on determining the vertical component of thermospheric winds providing a broad coverage for the study of neutral dynamics of the upper atmosphere.

In this thesis, neutral vertical wind data taken from Brazil FPI ground-based observations at around 240-km altitude between the years of 2010 to 2013 are used for a climatological study, which includes dependencies on seasonal and geomagnetic variations. First, in order to examine the reliability of the data, a cross-comparison from two different FPI measurement modes has been conducted. Second, the data have been

binned according to local time and month. Moreover, variations of vertical winds and neutral temperatures during two storm periods have also been studied. Vertical winds show statistically non-zero values at a given local time, while displaying upward shifts of 5 m/s during analyzed storm events. Neutral temperatures show an increase by 100-200 K on the duskside during the same analyzed storm events.

Table of Contents

Acknowledgements	iii
Abstract	iv
List of Figures.....	vii
List of Tables.....	viii
Chapter 1 Motivation	1
Chapter 2 Introduction	3
2.1 Thermospheric Winds	3
2.2 Transport Equations	6
2.3 The Thermosphere-Ionosphere System	9
2.4 Plasma Peak Formation	12
Chapter 3 FPI Observations	15
3.1 Detection of Thermospheric Winds.....	15
3.2 FPI Observation Comparison	19
3.3 The Zero-Laser Technique	23
Chapter 4 FPI Data Analysis.....	25
4.1 The experiment (Site)	25
4.2 Data Statistics and Validation	27
Chapter 5 Results and Discussion	31
5.1 Seasonal Variation of Vertical Winds.....	31
5.2 Vertical Wind and Temperature Variation During Storms.....	34
Chapter 6 Conclusion	39

6.1 Conclusion	39
6.2 Future Work	40
References.....	41
Biographical Information	43

List of Figures

Figure 1-1 Systems that can be affected by solar storms	2
Figure 2-1 Meteorological wind notations for thermospheric winds	4
Figure 2-2 Temperature bulge on the sunward side of the Earth	5
Figure 2-3 Comparison of the Jicamarca average drifts with thermospheric wind data from DE-2.....	5
Figure 2-4 Volume elements, d^3r about position vector r , and d^3v_s about velocity v_s vector in phase-space	6
Figure 2-5 Profile of the temperature (left) and plasma density (right) of the earth's atmosphere	11
Figure 2-6 Density profile of oxygen ion for the daytime F-region with the associated chemical and diffusive equilibrium profiles	14
Figure 3-1 Daytime concentration of atmospheric constituents	16
Figure 3-2 SkyScanner looking south in Cariri. Reprinted from Daniel Fisher's Thesis, University of Illinois at Urbana-Champaign	19
Figure 3-3 Global map of known working FPI sites until the year 2012	20
Figure 3-4 Research study on neutral vertical winds by Larsen & Meriwether et al. 2012	21
Figure 3-5 Research study on neutral vertical winds by Aruliah et al. 2005	21
Figure 3-6 Research study on neutral vertical winds by Sipler et al. 1995	22
Figure 3-7 (a) FPI Cardinal Mode, aerial view. (b) FPI Common Volume Mode	24

Figure 4-1 Geometry of the bi-static FPI experiment	25
Figure 4-2 Data Collected for Thermospheric Neutral Winds	27
Figure 4-3 Data Collected for Thermospheric Neutral Temperatures	28
Figure 4-4 F10.7 Index from Jan 2010 to Jul 2012	29
Figure 4-5 Summary of Vertical Wind Data Obtained from RENOIR System.....	30
Figure 4-6 Comparison of vertical winds between FPI cardinal mode and FPI common volume mode	30
Figure 5-1 Monthly climatologies of vertical winds in 2010. Green triangles represent data from the cardinal mode and magenta crosses from common volume (CV) mode	32
Figure 5-2 (a) Local time variation of average vertical winds in four different seasons for 2010. (b) Local time variation of average vertical neutral winds for the fall season in three for the years of 2010, 2011 and 2012	33
Figure 5-3 Dst, and Kp indices (top two panels), vertical winds and neutral temperature (bottom two panels) during Sept. 17th, 2011 storm	35
Figure 5-4 Dst, and Kp indices (top two panels), vertical winds and neutral temperature (bottom two panels) during Sept. 26th, 2011 storm	36
Figure 5-5 FPI measured vertical neutral wind and neutral temperature before (on September 16th) and during (on September 17th) storm period, which are represented by black line and red line, respectively	38
Figure 5-6 FPI measured vertical neutral wind and neutral temperature before (on September 25th) and during (on September 26th) storm period, which are represented by black line and red line, respectively	38

List of Tables

Table 2-1 Classification and nomenclature of the terrestrial atmosphere	10
Table 3-1 Organization of the ionosphere according to chemical composition	16
Table 3-2 Rate coefficients for the 630.0-nm emission.....	18
Table 4-1 Parameters concerning common volume geometry	26

Chapter 1

Motivation

For almost a century now, scientists have been studying the complex interaction between earth and space with the use of imaging systems such as Fabry-Perot interferometers (FPIs) and global positioning system receivers (GPS). Technology improvement has allowed more sites to be spread around the globe for atmospheric observation. At the same time, there are a growing number of users of communication satellites, and other technologies that can be affected by the state of the upper atmosphere. This growth of technology translates into more people being affected by space weather. Power grid stations, long-distance communication systems, satellites, and astronauts to name a few, all can be disturbed or harmed by solar storms. These disturbances can even result in catastrophic consequences such as the power outage suffered in Quebec in 1989, where millions of people suddenly found themselves in the dark. In order to observe such disturbances and ultimately correctly predict them, it is important to be constantly observing our atmosphere. Figure 1-1 shows the various systems that can be affected by solar storms.

Even though scientists have been gathering data from various instruments both in space and around the globe to accurately model the upper atmosphere, such models are still far from being perfect. Space scientists need more data collected by instruments to come up with better space weather models. The scientific community hopes to fully understand the complex space-earth environment through these models so that engineers can design satellites and power equipment that are less affected by storms. A bi-static FPI system has been operating in northeastern Brazil since 2009 to measure the 630.0-nm redline emission of atomic oxygen in the F-region ionosphere. In this thesis, this bi-static FPI system data collection is used to analyze the variations of vertical winds

and neutral temperatures with season and geomagnetic activity in order to better describe the neutral dynamics of the upper atmosphere.

To begin this study, Chapter 2 examines the basic characteristics of thermospheric winds as well as the interaction of the neutral gas with the ions in what is called the Thermosphere-Ionosphere (TI) system. Chapter 3 covers the FPI instrumentation located at two different cities, Carari and Cajazeiras, in northeastern Brazil. In addition, some FPI observations that have been made in other studies are mentioned. Chapter 4 describes the data analysis of vertical winds and temperatures. Validation of the data is also studied. Chapter 5 shows the results obtained from the data analysis by showing neutral vertical wind and temperature variations with season and storms. Finally, Chapter 6 gives some conclusions based on previous results obtained.

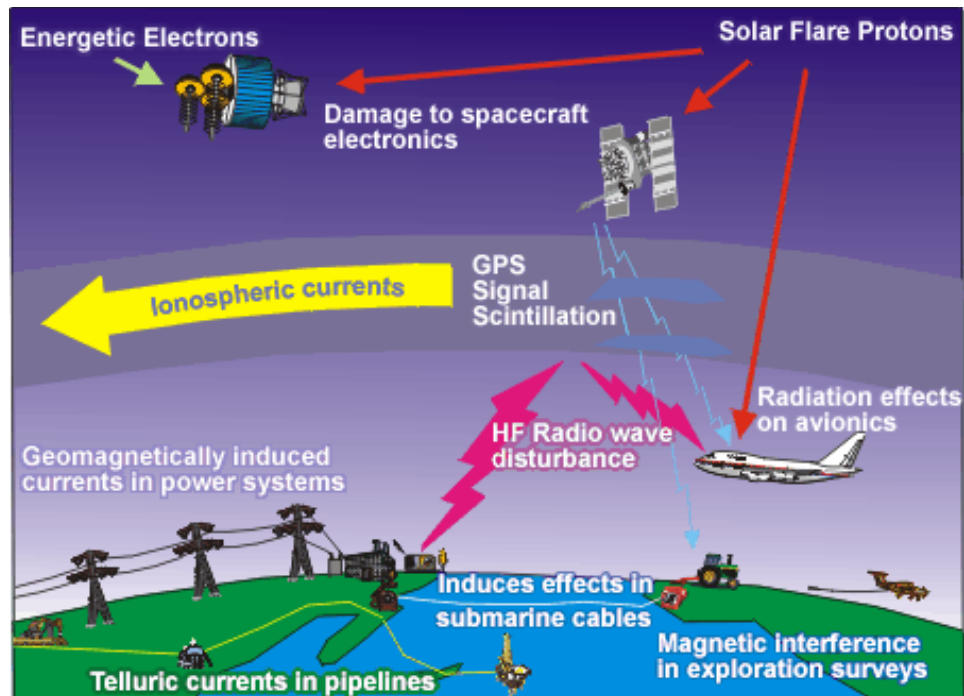


Figure 1-1 Systems that can be affected by solar storms.

Chapter 2

Introduction

This chapter introduces some background covering thermospheric winds and the interaction between the neutral and ionized portion of the atmosphere to give a basis for the science described in further chapters. It provides an overview of how thermospheric winds are produced and some of its effects on the upper atmosphere, as well as description of the process that leads to ionization peak formation.

2.1 Thermospheric Winds

The temperature bulge that occurs on the sunward side of the earth, Figure 2-2, creates a large pressure gradient that leads to wind motion across the sunset terminator. From this general description, which applies to a low-latitude thermosphere, we can state that winds, along the equator, blow in the negative pressure gradient direction, that is, from west to east. This statement is supported by early observational data on thermospheric winds [7]. Analysis of such data shows that the neutral atmosphere exerts a drag force on artificial satellites which causes their inclination to change. The interesting conclusion was that, the low-latitude thermosphere super-rotates, which means that there is a net eastward zonal flow of about 150 m/s near 350-km of altitude [1]. Figure 2-3 shows the comparison of the Jicamarca average drifts with thermospheric wind data from DE-2 [8]. Note from this figure that winds can be as high as 150 m/s right before midnight, and that they change direction from west to east around sunset confirming the net eastward wind flow.

Thermospheric neutral winds can strongly influence the upper atmosphere by redistributing heat and momentum and by changing the neutral composition and electrodynamic processes. In particular, vertical winds can have a very important

influence on the upper atmosphere because of the large vertical density gradients that exist throughout the atmosphere. Although vertical winds are significantly smaller than typical zonal and meridional winds, they can be non-zero under certain conditions. Thus, this vertical circulation can result in a strong disturbance of the neutral density which dramatically can alter low-altitude satellite orbits by increasing the atmospheric drag on the satellites.

Moreover, to be well equipped for thermospheric wind analysis, a practical wind notation needs to be established for mathematical purposes. Most commonly, the meteorological wind notation is the preferable one. Following this meteorological notation, the wind vector is represented by

$$(u,v,w) = (\text{East}, \text{North}, \text{Zenith}) = (\text{zonal}, \text{meridional}, \text{vertical})$$

This wind vector is graphically represented in Figure 2-3. These vectors (East, North, Zenith) are orthogonal to each other such as the more common vectors (x,y,z) in a 3-dimensional space. Note that East vector is pointing into the page so as to make 90-degree angles with the other two vectors.

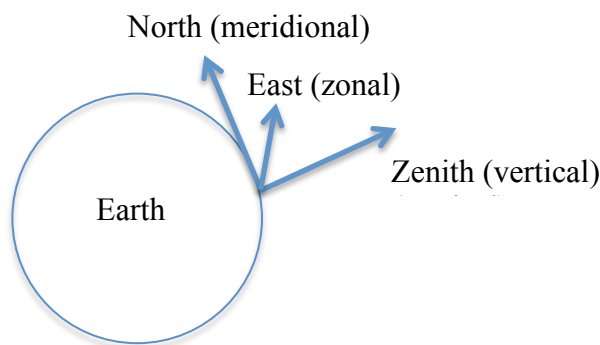


Figure 2-1 Meteorological wind notations for thermospheric winds.

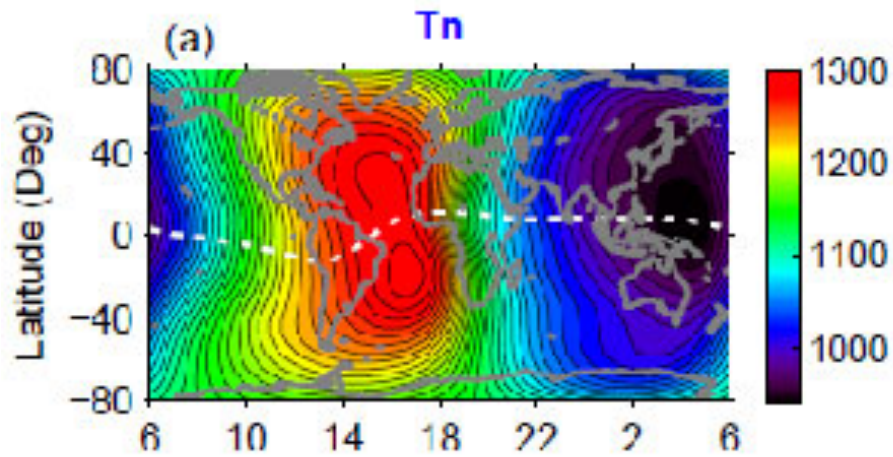


Figure 2-2 Temperature bulge on the sunward side of the Earth.

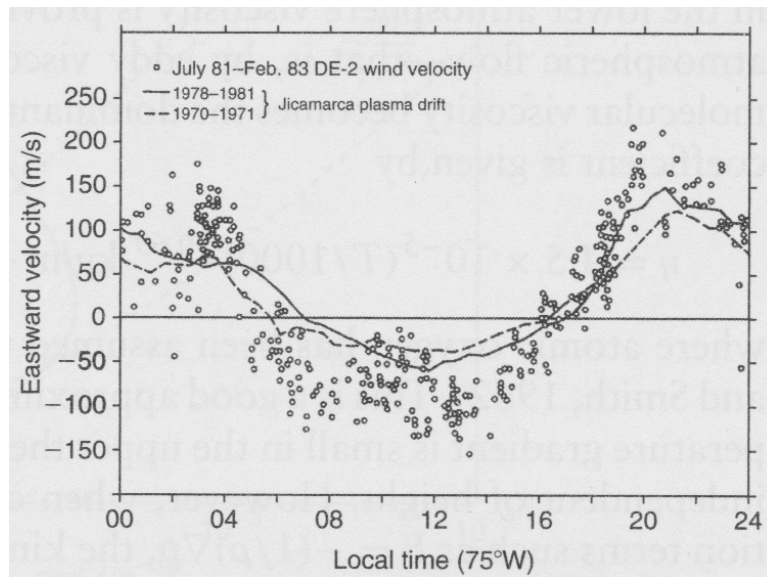


Figure 2-3 Comparison of the Jicamarca average drifts with thermospheric wind data from DE-2. Reprinted from The Earth's Ionosphere, Kelley, Page 77, 1989 [1].

2.2 Transport Equations

Before discussing the interaction between neutrals and ions in the upper atmosphere in what is known as the Thermosphere-Ionosphere system, transport equations, such as the continuity and momentum equations are described in order to better understand what forces drive the gas species at ionospheric altitudes. The starting point for the derivation of transport equations is the Boltzmann equation. In this approach, the motion of a distribution of particles is of interest as opposed to following the flow of individual particles [2].

The following mathematical approach is based on the work of Nagy & Shunk, reference [2]. Each gas species is described by a separate velocity distribution function $f_s(\mathbf{r}, \mathbf{v}_s, t)$, where \mathbf{r} , \mathbf{v}_s and t are independent variables. Particles of the gas species s are located in a volume element d^3r about \mathbf{r} with velocities in a velocity-space volume element d^3v_s about \mathbf{v}_s , Figure 2-4. The rate of change of the distribution function f_s due to an explicit time variation and a flow in phase-space is given by

$$\frac{df_s}{dt} = \lim_{\Delta t \rightarrow 0} \frac{f_s(\vec{r} + \Delta\vec{r}, \vec{v}_s + \Delta\vec{v}_s, t + \Delta t) - f_s(\vec{r}, \vec{v}_s, t)}{\Delta t} \quad (2.1)$$

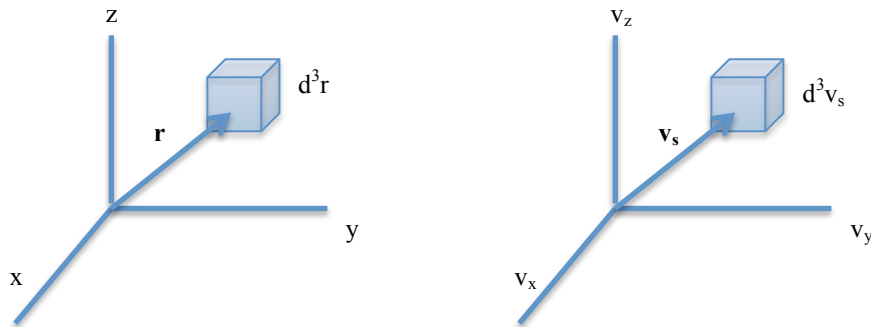


Figure 2-4 Volume elements, d^3r about position vector \mathbf{r} , and d^3v_s about velocity vector \mathbf{v}_s in phase-space [2].

Since Δt is a small quantity, the function $f_s(\vec{r}+\Delta\vec{r}, \vec{v}_s+\Delta\vec{v}_s, t+\Delta t)$ can be expanded in a Taylor series as follows

$$\begin{aligned} \frac{df_s}{dt} = \lim_{\Delta t \rightarrow 0} \frac{1}{\Delta t} [& f(\vec{r}, \vec{v}_s, t) + \frac{\partial f_s}{\partial t} \Delta t + \Delta\vec{r} \cdot \nabla f_s \\ & + \Delta\vec{v}_s \cdot \nabla_{\vec{v}_s} f_s + \cdots - f_s(\vec{r}, \vec{v}_s, t)] \end{aligned} \quad (2.2)$$

By taking the limit as $\Delta t \rightarrow 0$, (2.2) becomes

$$\begin{aligned} \frac{df_s}{dt} = \frac{\partial f_s}{\partial t} + \vec{v}_s \cdot \nabla f_s + \vec{a}_s \cdot \nabla_{\vec{v}_s} f_s \end{aligned} \quad (2.3)$$

where $\nabla_{\vec{v}_s}$ is the gradient operator in velocity space

and all higher-order terms have been dropped, and the following definitions were used

$$\begin{aligned} \frac{\Delta\vec{r}}{\Delta t} &\rightarrow \frac{d\vec{r}}{dt} \rightarrow \vec{v}_s \\ \frac{\Delta\vec{v}_s}{\Delta t} &\rightarrow \frac{d\vec{v}_s}{dt} \rightarrow \vec{a}_s \end{aligned} \quad (2.4)$$

If collisions between particles are not important, then the left hand side of (2.3) becomes zero, $df_s/dt = 0$, resulting in *Vlasov equation*. Nevertheless, when collisions become important such as in a medium where ions and neutrals can interact with each other (Thermosphere-Ionosphere system), then we get *Boltzmann equation* given by

$$\frac{\partial f_s}{\partial t} + \vec{v}_s \cdot \nabla f_s + \vec{a}_s \cdot \nabla_{\vec{v}_s} f_s = \frac{\delta f_s}{\delta t} \quad (2.5)$$

where the term on the right-hand side, $\delta f_s/\delta t$, has been used to define the collisions.

Transport equations can be obtained by multiplying the Boltzmann equation (2.5) with an appropriate function of velocity and then integrating over velocity space. The result of this mathematical process leads to the continuity and momentum transport equations.

Applying this procedure on both sides of equation (2.5) results in the following

$$\begin{aligned}\int d^3v_s \frac{\partial f_s}{\partial t} &= \frac{\partial}{\partial t} \int d^3v_s f_s = \frac{\partial n_s}{\partial t} \\ \int d^3v_s \nabla \cdot (f_s \vec{v}_s) &= \nabla \cdot \int d^3v_s f_s \vec{v}_s = \nabla \cdot (n_s \vec{u}_s) \\ \int d^3v_s \frac{\delta f_s}{\delta t} &\equiv \frac{\delta n_s}{\delta t}\end{aligned}\tag{2.6}$$

Thus, the continuity equation becomes

$$\frac{\partial n_s}{\partial t} + \nabla \cdot (n_s \vec{u}_s) = \frac{\delta n_s}{\delta t}\tag{2.7}$$

Similarly, following the same method of multiplying (2.5) by functions of velocity and integrating over velocity space, the momentum equation becomes

$$n_s m_s \frac{D_s \vec{u}_s}{Dt} + \nabla \cdot \vec{P}_s - n_s m_s \vec{G} - n_s e_s (\vec{E} + \vec{u}_s \times \vec{B}) = \frac{\delta \vec{M}_s}{\delta t}\tag{2.8}$$

where $\frac{D_s}{Dt} = \frac{\partial}{\partial t} + \vec{u}_s \cdot \nabla$ is the convective derivative

\vec{P}_s is the pressure tensor, \vec{G} is gravity acceleration

\vec{E} is the electric field, and \vec{B} is magnetic field

and where the following relations have been used

$$\begin{aligned}m_s \int d^3v_s (\vec{v}_s - \vec{u}_s) \frac{\partial f_s}{\partial t} &= n_s m_s \frac{\partial \vec{u}_s}{\partial t} \\ m_s \int d^3v_s (\vec{v}_s - \vec{u}_s) \nabla \cdot (f_s \vec{v}_s) &= \nabla \cdot \vec{P}_s + n_s m_s (\vec{u}_s \cdot \nabla) \vec{u}_s \\ m_s \int d^3v_s (\vec{v}_s - \vec{u}_s) \frac{\delta f_s}{\delta t} &\equiv \frac{\delta \vec{M}_s}{\delta t}\end{aligned}\tag{2.9}$$

These transport equations, (2.7), and (2.8) can be used to model several different flow conditions, either collision-dominated flows or collisionless flows, encountered in planetary ionospheres [2].

2.2 The Thermosphere-Ionosphere System

The neutral atmosphere can be neatly organized by a representative temperature profile, whereas the ionized portion of the atmosphere, the ionosphere, is organized by the number density of plasma. Starting with the neutral atmosphere, in the troposphere, the layer closest to the ground, the temperature decreases with increasing height and at around 10-km of altitude there is a reversal in temperature, this marks the beginning of the next atmospheric layer, the stratosphere. In this second layer the temperature increases with height due to the absorption of ultraviolet radiation by ozone, and at around 50-km of altitude there is another temperature change, marking the beginning of the mesosphere. Radiative cooling in this layer causes the temperature to decrease to a minimum value in the range of 130-190 K, and at about 90-km of altitude we have the last temperature change. For heights above 90-km where the temperature is at its minimum (mesopause), the temperature increases dramatically due to the absorption of high energy solar photons up to a constant value of approximately 1500K. This region of very high temperature is called the thermosphere. Also, the atmosphere is relatively uniform in composition below about 100-km due to the turbulent mixing phenomena. Above the so-called "turbopause" the constituent gas begins to separate according to its mass.

Table 2-1 shows the structure of the neutral atmosphere according to different heights. It can be seen from this table that below 100-km altitude, atmospheric gases are well mixed giving a homogeneous atmospheric composition, whereas above this altitude gases tend to separate into its constituents forming a more heterogeneous atmosphere.

Turning now attention to the ionosphere, and because of its ionized state, the ionosphere is divided according to its plasma density with respect to different heights. The ionospheric plasma is produced by Extreme UltraViolet (EUV) solar radiation which has the energy required to knock out electrons from the neutral gas producing positively

charged ions and free electrons. The plasma content per volume (density) varies with height due to the varying energy of solar radiation as it travels deeper into the atmosphere and interacts with neutral gas constituents. The starting point of the ionosphere is the height where the number of ionized constituents per volume starts to become important which usually falls around 10^3 particles per volume. Figure 2-4 shows typical profiles for the neutral (left) and ionized (right) gases of the atmosphere.

Table 2-1 Classification and nomenclature of the terrestrial atmosphere.

100,000	Interplanetary Space		
10,000	Exobase	Hydrosphere (Geocorona)	Plasmasphere (Protonosphere)
1,000		Heterosphere (separated gases)	
	Thermosphere		F-Region
100	Mesopause	Homopause	E-Region
	Mesosphere		D-Region
50	Stratopause	Homosphere (well mixed gases)	
	Stratosphere		
10	Tropopause		
0	Troposphere		
Height (km)	Layer	Composition	Plasma Region

This starting point of the ionosphere is called the D-region, then it goes alphabetically as the plasma density increases with height, it follows E-region, and finally we get to the F-region where the plasma density reaches a maximum. Equal numbers of positive ions and electrons are produced in the ionization process along the different ionospheric regions, this is a requirement for a gas to be termed a plasma, that is, the combination of negative and positive particles very nearly satisfies neutrality. Thus, at ionospheric heights $n_i \approx n_e \approx n$ is assumed to hold. However, if n_i is exactly equal to n_e everywhere, then there would be no electrostatic fields at all, which is not the case [1].

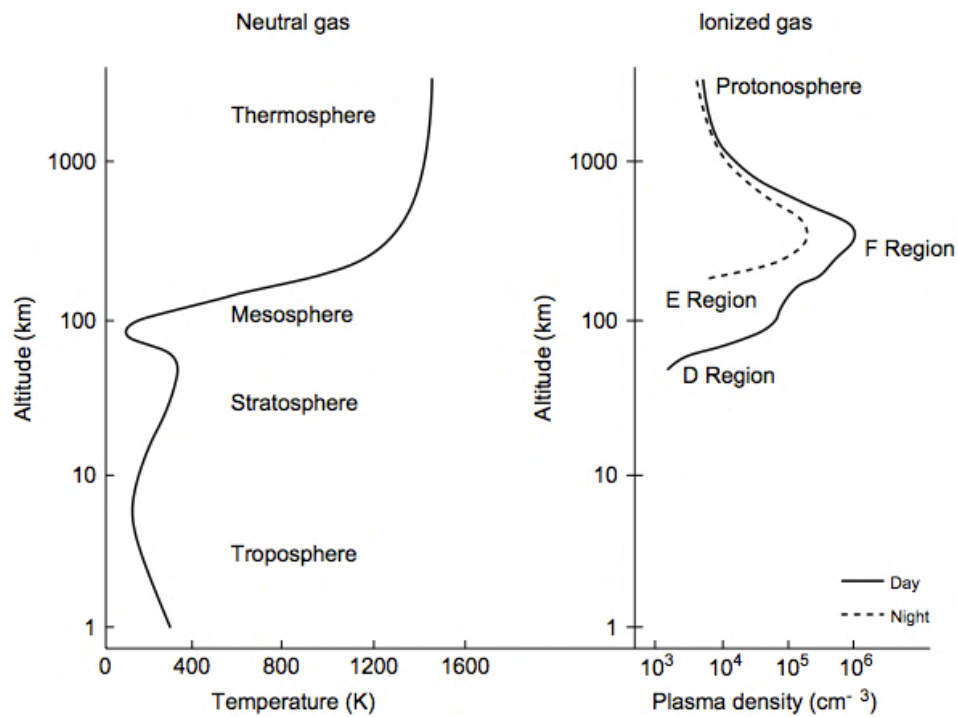


Figure 2-5 Profile of the temperature (left) and plasma density (right) of the earth's atmosphere. Reprinted from The Earth's Ionosphere, Kelley, Page 5, 1989 [1].

Going back to the Thermosphere-Ionosphere (TI) system, we can see from Figure 2-4 that the TI system is the region where the thermosphere and ionosphere coincide within a certain altitude range $\sim (100-1000)$ -km, and where neutrals from the thermosphere can interact with ions from the ionosphere giving important information about the neutral dynamics of the upper atmosphere which will be discussed in later sections.

2.3 Plasma Peak Formation

In order to describe the plasma F-peak formation that occurs at around 300-km altitude (see Figure 2-4) two different processes need to be taken into account, chemical equilibrium, below the peak, and diffusion equilibrium above the peak. Starting from below the peak, the dominant process that the gas species follow in this region is chemical equilibrium, where the major ion at these F-region altitudes is given by O^+ , and the density of the gas can be described as the ratio of the production rate $P_s(O^+)$ to the loss rate $L_s(O^+)$ of this major O^+ ion, and given by the following equation

$$n(O^+) = \frac{P_s(O^+)}{L_s(O^+)} = n_0(O^+) \frac{\exp\left[\frac{-(z - z_0)}{H_o}\right]}{\exp\left[\frac{-(z - z_0)}{H_{N_2, O_2}}\right]} \quad (2.10)$$

where H_o and H_{N_2, O_2} are the scale heights for Oxygen, diatomic Nitrogen and Oxygen, respectively, and z, z_0 are reference altitudes. But the densities of molecular atoms, N_2, O_2 , decrease much faster with height than the density of atomic oxygen, O [2], so the denominator of (2.1) will decrease much faster than the numerator giving an overall exponentially increasing function. Thus, (2.1) becomes

$$n(O^+) = n_0(O^+) \exp\left(\frac{z - z_0}{H_{pl}}\right) \quad (2.11)$$

where the effective scale height is defined as

$$H_{pl} = \frac{kT}{(M_{N_2,O_2} - M_O)m_u g} \quad (2.12)$$

and where k is Boltzmann's constant, T is the temperature of the gas, M_{N_2,O_2} is the molecular mass of diatomic-Nitrogen (N_2) and diatomic-Oxygen (O_2), m_u is the effective mass of total gas system, and g the gravity constant.

Furthermore, in the region above the peak, the dominant process that the gas species follows is diffusive equilibrium. The derivation of the equation for a diffusive process can be as follows. Consider the case where the pressure gradient and gravitational forces acting on an ion gas and its associated electron gas are in equilibrium. This leads to the hydrostatic equation which is given by

$$\frac{dp_s}{dz} = -\rho_s g \quad (2.13)$$

where ρ_s is the density of the gas species, and g is gravity constant. Moreover, if we do a force balance relation for ions and electrons using (2.4) plus an electric force term, we can get the following two equations

$$\begin{aligned} \frac{dp_i}{dz} &= -\rho_i g + n_i e E_p \\ \frac{dp_e}{dz} &= -\rho_e g - n_e e E_p \end{aligned} \quad (2.14)$$

where e is the electric charge and E_p is the electric polarization field. Next, assuming that the electric polarization field is strong enough to enforce charge neutrality, i.e., $n_i \approx n_e = n$, which is in agreement with observations [6], then by adding equations (2.5) we obtain

$$\frac{d(p_i + p_e)}{dz} \cong -nm_i g \quad (2.15)$$

where the electron mass can be neglected, i.e., $m_e \ll m_i$, in relation to the ions mass. Finally, equation (2.6) can be integrated and the following expression for the density above the peak is obtained

$$n_i = (n_i)_0 \exp\left(-\frac{z - z_0}{H_p}\right) \quad (2.16)$$

with the scale height H_p given by

$$H_p = \frac{k(T_i + T_e)}{m_i g} \quad (2.17)$$

where T_i and T_e are the ion and electron temperatures, respectively.

Thus, it can be seen from the solution above the peak (2.7) that the density decreases exponentially. The intersection of the two solution exponential functions (2.2) and (2.7), determines the plasma F-peak at around 300-km altitude and shown in Figure 2-5.

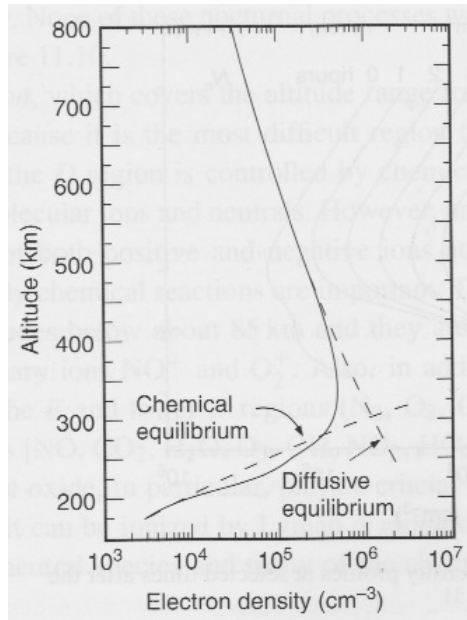


Figure 2-6 Density profile of oxygen ion for the daytime F-region with the associated chemical and diffusive equilibrium profiles [2].

Chapter 3

FPI Observations

In this chapter a description of how thermospheric winds can be detected with ground-based observational techniques such as the Fabry-Perot Interferometer (FPI) experiment is given. Then, several observational analysis from other previous research are mentioned as a way of having a comparative for this current research topic. Finally, a brief description of the modes of operation for the FPI instrumentation are mentioned.

3.1 Detection of Thermospheric Winds

Now that we have a general idea on how these winds can be produced, and now that we know that neutrals can coincide with ions, the question is, How can we detect and measure these neutral atmospheric winds? In order to answer this question, we need to go back to the Thermosphere-Ionosphere system and identify major ions and neutrals that coincide within the TI system altitude range.

Scientists found out that interactions between major neutrals and ions give off light emissions that can actually be detected from ground-based instruments during the night. These upper atmospheric reactions are referred to as airglow emissions and have a peak at an altitude of around 240-km. Figure 3-1 gives density profiles of the major ions and neutrals that occur at this desired emission peak altitude. From this figure we can see that the major ions at this altitude peak are atomic oxygen O^+ , molecular oxygen O_2^+ , and molecular nitrogenous oxygen NO^+ , whereas major neutrals are given by atomic oxygen O , molecular nitrogen, N_2 , and molecular oxygen O_2 .

Furthermore we can organize major ions according to the corresponding ionospheric regions. Table 3-1 shows this dominant ion organization with respect to different ionospheric layers.

Table 3-1 Organization of the ionosphere according to chemical composition.

Ionosphere	D-region	$h < 90 \text{ km}$	$\text{H}_3\text{O}^+(\text{H}_2\text{O}), \text{NO}_3^-$
	E-region	$90 < h < 150 \text{ km}$	$\text{O}_2^+, \text{NO}^+$
	F-region	$150 < h < 1000 \text{ km}$	O^+
Plasmasphere	$h > 1000 \text{ km}$		H^+

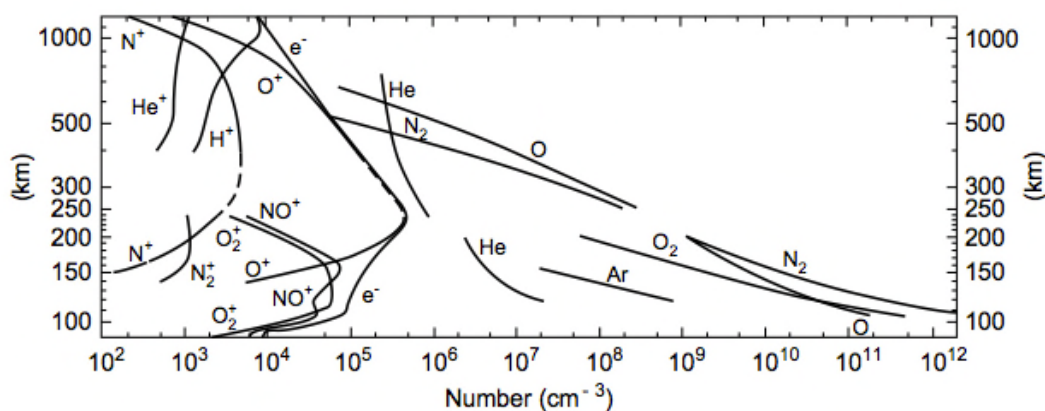
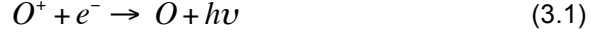
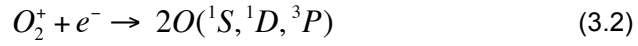


Figure 3-1 Daytime concentration of atmospheric constituents. Reprinted from The Earth's Ionosphere, Kelley, Page 6, 1989 [1].

Oxygen being a major neutral (see Figure 3-1) at the height of interest (~240- km) is involved in the emission of three commonly used airglow lines, 557.7 nm, 630.0 nm, and 777.4 nm. The 557.7-nm greenline emission is a bright, short-lived reaction (0.74-s lifetime), but occurs in the mesosphere, which is below the region of interest. The 777.4 nm emission is due to the radiative recombination of ionized oxygen, and is described by the following reaction [1]



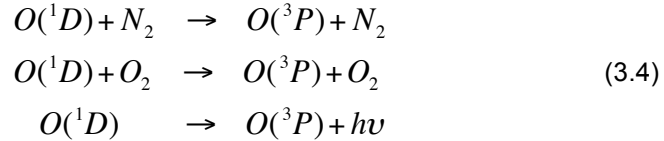
but reaction (3.1) occurs only with plasmas (no neutral winds measured). Thus, the 630.0-nm redline emission is chosen to study the neutral thermosphere-ionosphere system. The 630.0-nm emission is produced through the dissociative recombination of O_2^+ in the following way



The $O(^1D)$ excited state, which emits the 630.0-nm photon, is created in a fraction of the time it takes for the O_2^+ to form. The production of O_2^+ occurs through an ion exchange reaction with an ionized oxygen atom



Moreover, before a photon is emitted, three reactions cause the excited state oxygen atom to be depleted



The first two reactions shown in (3.2) are known as quenching reactions, whereas the third reaction is spontaneous recombination. The total estimated intensity of the redline emission is on the order of 100 Rayleighs. This can intensity can be calculated from the following equation [10]

$$k_{630.0} = \frac{0.76A_{1D}\beta_1k_1[O^+][O_2]}{A_{1D} + k_3[N_2] + k_4[O_2] + k_5[e^-]} \quad (3.5)$$

Coefficients of the 630.0-nm reaction are given in Table 3-2. This 630.0-nm emission rate shows that is affected by both the plasma part as well as the neutral part of the upper atmosphere, hence by the thermosphere-ionosphere system. The redline emission peak which occurs around 240-km altitude is due to the balance between ion and neutral concentrations. If the plasma density decreases in the ionosphere, the decreased concentration of electrons and O^+ ions will decrease the emission rate. Also, less signal intensity could be due to the F peak rising in altitude; hence, fewer available neutrals leading to less recombination with decreasing signal strength.

Table 3-2 Rate coefficients for the 630.0-nm emission [10].

Coefficient	Rate	Units
A_{1D}	6.81_{E-3}	1/s
β_1	1.1	
k_1	$3.23_{E-12} \exp(3.72/T_i - 1.87/\tau^2)$	cm^3/s
k_3	$2.0_{E-11} \exp(111.8/T_n)$	cm^3/s
k_4	$2.9_{E-11} \exp(67.5/T_n)$	cm^3/s
k_5	$1.6_{E-12} T_e^{0.91}$	cm^3/s
T_i / T_e	Ion/Electron Temperature	K
T_i	$T_i/300$	
T_n	Neutral Temperature	K

Camera detectors are placed on the FPI instrument to detect the red light emission of atomic oxygen at ionospheric heights. These camera detectors are shown in Figure 3-2.



Figure 3-2 SkyScanner looking south in Cariri. Reprinted from Daniel Fisher's Thesis, University of Illinois at Urbana-Champaign, Page 22, 2013 [3].

The instrument shown in Figure 3-2 is one of two FPI instruments that are located at northeastern Brazil, and which operation is explained in more detail in section 3.3.

3.2 FPI Observation Comparison

A global map of FPI instrument site locations until 2012 is given in Figure 3-3 [3]. Three different research works on vertical winds are mentioned here as a means of having a comparative analysis on thermospheric vertical winds.

Starting with the research study done by Larsen and Meriwether et al. 2012, located at Poker Flat Alaska, this work shows that vertical winds can be very variable with 4-hour sustained downward vertical winds at the beginning of the night followed by upward 6-hour sustained upward vertical winds after midnight, see Figure 3-4.



Figure 3-3 Global map of known working FPI sites until the year 2012 [3].

Magnitudes of these thermospheric vertical winds were as high as 50 m/s. Another research study that shows highly variable winds is the research work done by Aruliah et al. 2005, located at a high-latitude site in Finland. This work shows oscillatory behavior of vertical winds with magnitudes reaching values as high as 100 m/s two hours before midnight, Figure 3-5. Finally, another important research work that can be mentioned is the work done by Sipler et al. 1995, at a mid-latitude site, northeastern region of U.S. Again, oscillatory behavior of neutral vertical winds can be seen for the three consecutive nights of the study, Figure 3-6. Though, Vertical wind magnitudes for this mid-latitude site had lower values of 20 m/s, on average.

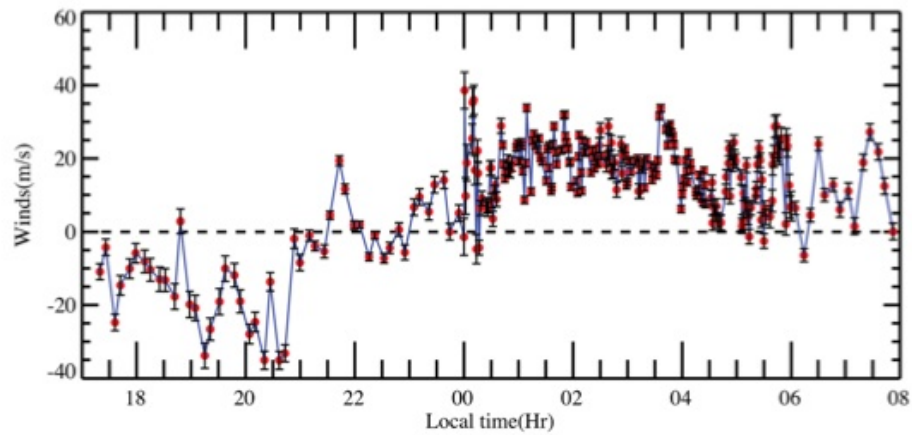


Figure 3-4 Research study on neutral vertical winds done by Larsen & Meriwether et al., 2012 [5].

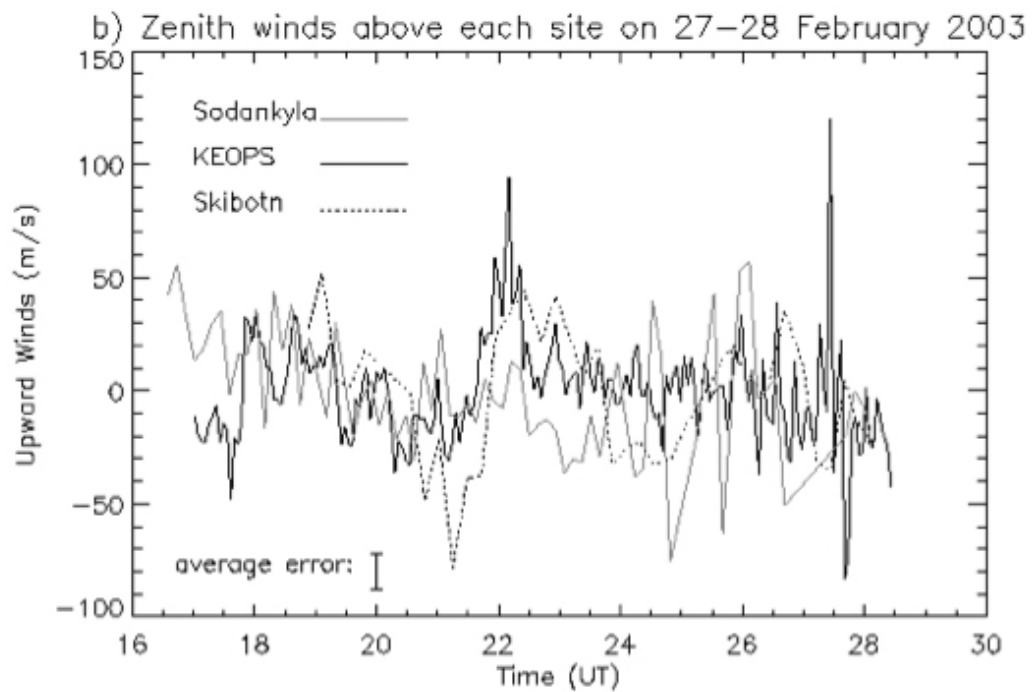


Figure 3-5 Research study on neutral vertical winds by Aruliah et al. 2005 [9].

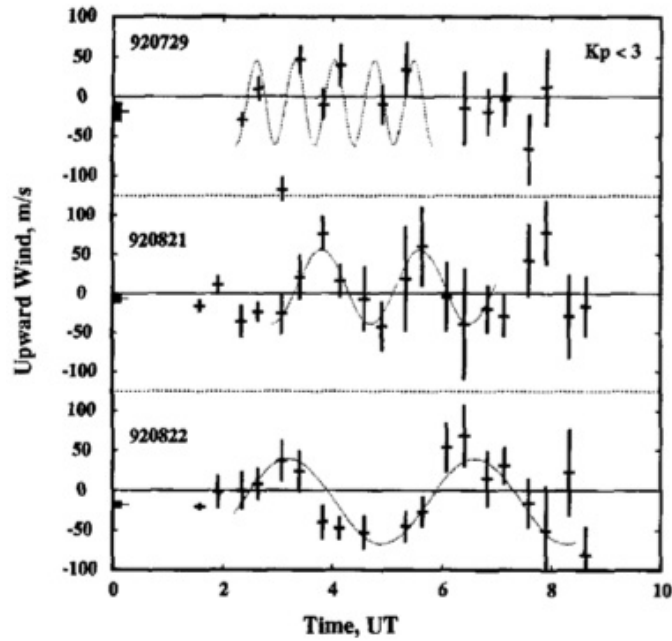


Figure 3-6 Research study on neutral vertical winds by Sipler et al. 1995 [12].

Even though, these previous thermospheric vertical wind research studies were done for higher-latitude sites, which usually give higher magnitude winds [1], all these studies prove the existence of large vertical winds for extended periods of time. However, vertical winds have not been observed systematically and the drivers for the observed events of large vertical winds are still not clear. For this reason, in this thesis, a climatological study of the equatorial F-region vertical winds has been conducted. More than three years data (2010- 2013) from the bi-static FPI observatory in equatorial Brazil have been utilized. But before going into the analysis of vertical thermospheric winds, a brief introduction into the operation modalities of the bi-static FPI system is discussed to understand how actual vertical winds are obtained and which data are the most reliable for use in the analysis.

3.3 The Zero-Laser Technique

A zero-reference level is needed in order for the FPI instruments to recognize the redline emission of atomic oxygen. A very straightforward method that scientist previously used to determine this zero reference was to assume vertical winds to be zero. Vertical winds (~10-20 m/s) are at least one order of magnitude less than horizontal winds (100-200 m/s), so the zero-vertical-wind assumption was a reasonable one by old equipment standards because the value of 0 m/s was contained within the measurement error bars. Each FPI instrument provides an estimate of the Line Of Sight (LOS) Doppler shift, which must be transformed into a useful coordinate system, such as east, north, and up. Doppler shifts can then be calculated as sum of projections of the u, v, w winds onto the observation direction measured by the instrument. The total Doppler velocity is defined as follows

$$V_i^{LOS} = w \sin(\alpha_i) + [v \cos(\theta_i) + u \sin(\theta_i)] \cos(\alpha_i) + \beta_i \quad (3.6)$$

where V is the observed velocity, β is the velocity offset due to the unknown Doppler reference, θ , and α are the azimuth and elevation angles, respectively, Figure 3.7. From equation (3.2) we can see that there are four unknowns. Zenith and inline FPI measurements eliminate the horizontal components, leaving still two unknowns. Thus, an undetermined system results. Two techniques can be used to make this system solvable. The first technique was already mentioned, the zero vertical wind assumption. But from previous studies on thermospheric vertical winds we have seen that vertical winds can be highly variable at a given local time (Chapter 3), so another technique that allows non-zero vertical winds must be chosen. The next approach to take is to use a HeNe-laser technique as a zero-reference for the Doppler shift and to take only average vertical

winds to be zero over the entire night of observation, which is a less restrictive assumption and allows for the possibility of non-zero vertical winds at a given local time.

Furthermore, modern FPI instruments are more accurate and have smaller measurement uncertainties and, therefore, should be able to measure vertical winds [3]. The frequency-stabilized HeNe laser technique allows the non-zero vertical wind possibility by providing an extra parameter called the beta (β) parameter. This beta parameter gives an extra piece of information that helps solve completely equation (3.2) enabling all wind components (u, v, w) to be determined at any given local time.

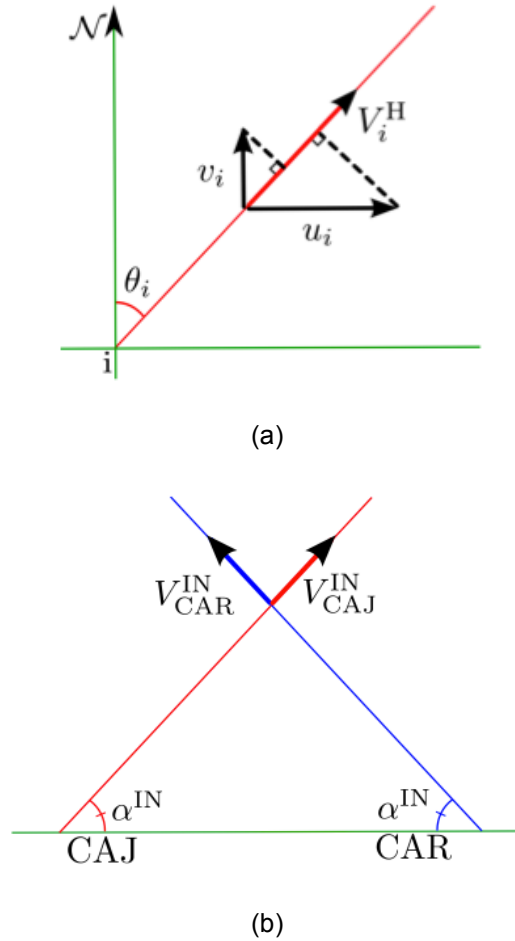


Figure 3-7 (a) FPI Cardinal Mode, aerial view. (b) FPI Common Volume Mode [3].

Chapter 4

FPI Data Analysis

In this chapter, the site where FPI instruments are located is discussed and the actual data obtained from these instruments is presented. In order to validate the data and make sure we are not dealing with possible instrumental contamination, a cross comparison between the two FPI operational modes (Section 3.3) is conducted and results of this validation method is presented as well.

4.1 The Site

In 2009, two RENOIR (Remote Equatorial Nighttime Observatory for Ionospheric Regions) systems were deployed in northeastern Brazil to monitor the thermosphere near the equator [4]. One FPI was placed at Cajazeiras, Brazil (CAJ, 6.871S, 38.561W), and another FPI was installed at Carari, Brazil (CAR, 7.381S, 36.521W). These two sites are separated by approximately 230-km in longitude, and are about 6° south of the equator.

The general geometry of the bi-static system is shown in Figure 4-1.

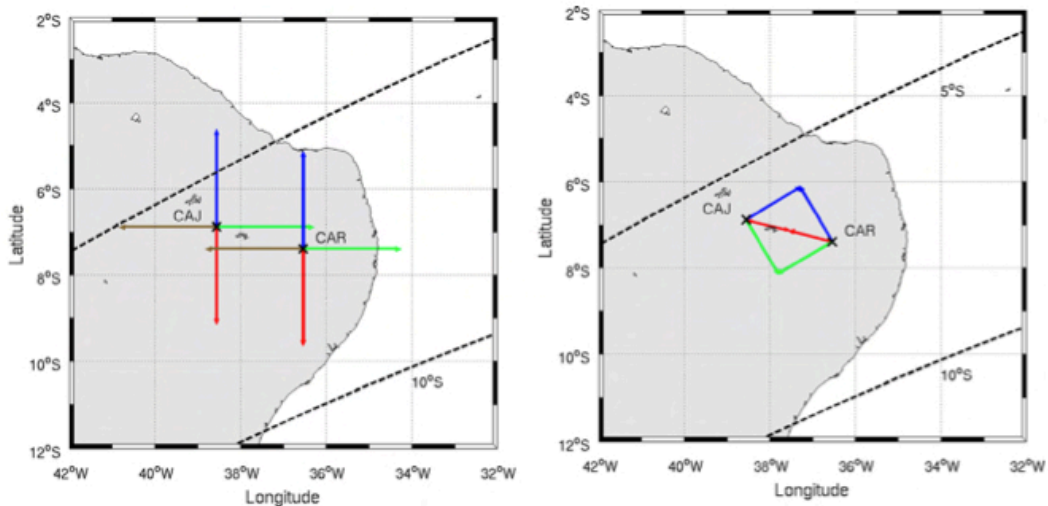


Figure 4-1 Geometry of the bi-static FPI experiment [4].

Observation directions for the cardinal mode (left panel, Figure 4-1) are shown by arrows. The tips of the arrows represent the latitude/longitude of the 240-km height from which the signal is assumed to come ([3], [4]). The instruments were set to operate in common volume mode as well (right panel, Figure 4-1). Some parameters concerning this common volume (CV) geometry are given in Table 4-1([3], [5]).

Table 4-1 Parameters concerning common volume geometry [3].

	From CAJ	From CAR
Elevation Angle to CVN	55.6°	55.6°
Azimuth Angle to CVN	59.1°	329.1°
Distance to CVN	164.25 km	164.25 km
Elevation Angle to IN	64.2°	64.2°
Azimuth Angle to IN	104.1°	284.1°
Distance to IN	116.14 km	116.14 km
Elevation Angle to CVS	55.6°	55.6°
Azimuth Angle to CVS	149.1°	239.1°
Distance to CVS	164.25 km	164.25 km

This CV mode of operation consists of a laser and zenith measurement sequence followed by one or two common volume points and the inline point. The midpoint (inline) is located at 7.13°S, 37.54°W (geomagnetic: 6.28°S, 33.84°E). The north common volume point (denoted CVN) is located at 6.11°S, 37.29°W (geomagnetic: 5.26°S, 34.45°E) while the south common volume point (denoted CVS) is located at 8.14°S, 37.80°W (geo- magnetic: 6.95°S, 33.22°E), [3]. These common volume points are shown

in Figure 4-1 (right panel), where the arrow tip indicates the point where the observation reaches 240 km in altitude. The two FPIs operate every night through a set of automated scripts [3]; instruments begin to take data after sunset and run until dawn. The actual data detected by this bi-static FPI system is discussed next.

4.2 Data Statistics and Validation

Data taken from the bi-static FPI system is presented in Figure 4-2 for thermospheric neutral winds obtained during Jan 2010 to Jul 2012. To create this plot, each night's observations are plotted as a function of local time on the y-axis with the date of the observation given by the x-axis [4]. In a similar way, thermospheric neutral temperatures were plotted and are shown in Figure 4-3. Zonal winds (positive eastward) are shown in the top panel and meridional winds (positive northward) are shown below.

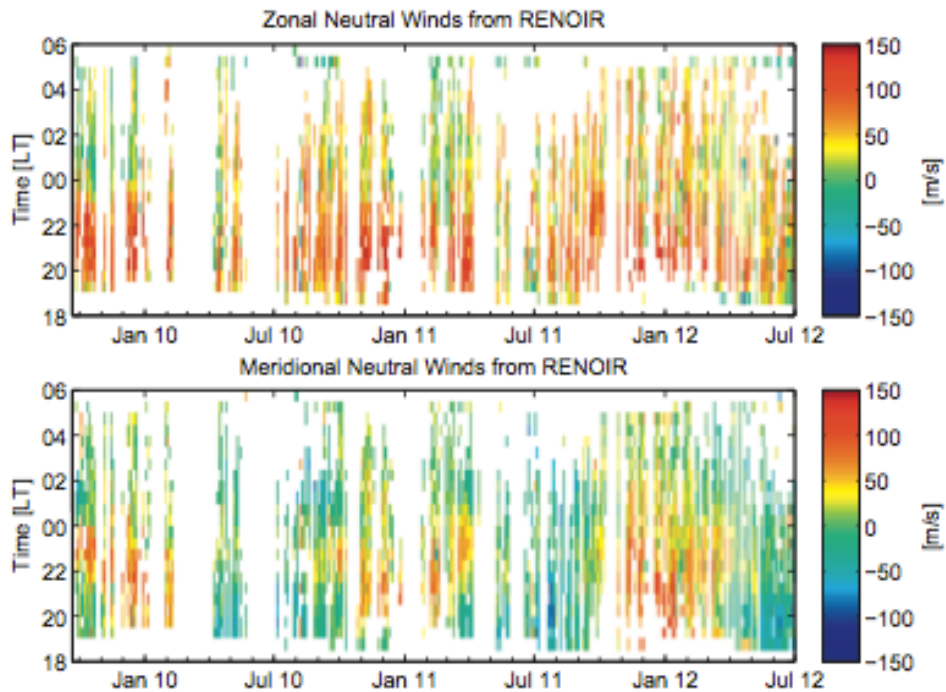


Figure 4-2 Data Collected for Thermospheric Neutral Winds [4].

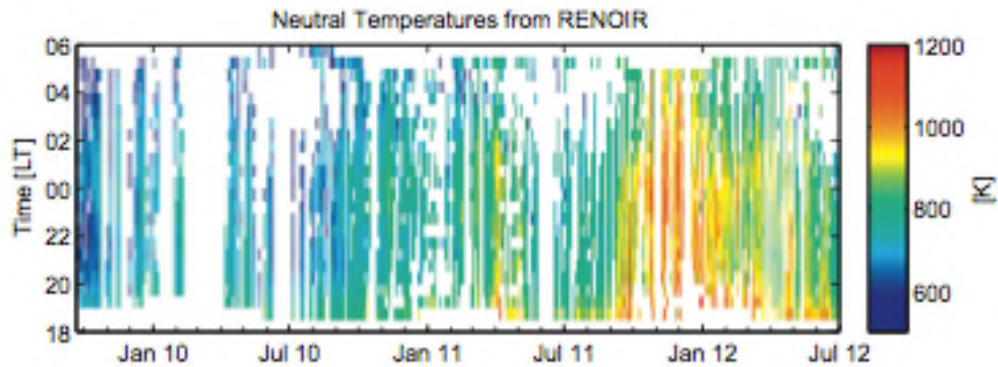


Figure 4-3 Data Collected for Thermospheric Neutral Temperatures [4].

Measurement points were discarded from the analysis if they had a statistical uncertainty larger than 75K or had values outside the range of 500–1400 K [4]. Similar to selecting data points for temperatures, winds were discarded if their statistical uncertainty was greater than 50 m/s or had values outside the range -200 to 200 m/s [4]. Also, to ensure uniformity in the analysis [4], if a temperature measurement was discarded, its corresponding wind value would be discarded as well, and vice versa.

In general, from Figures 4-2 and 4-3 there are several observations that can be made in order to be in a good position to judge the validity of the data. First, a temperature decrease is seen throughout the night. Second, a temperature increase can be associated with an increase of a F10.7 index for measuring solar flux conditions and that is shown in Figure 4-4. Third, zonal winds are seen to increase towards east after sunset followed by a decrease in magnitude at dawn, which is the expected behavior according to previous studies (see section 2.1). Finally, meridional winds display the expected trans-equatorial flow. Hence, all these observations give physically reasonable parameter behaviors and trends that provide confidence into further use of the data obtained from the bi-static FPI experiment.

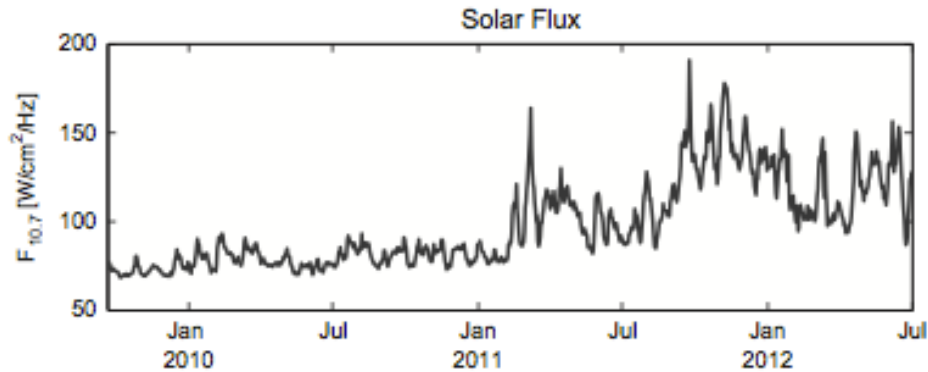


Figure 4-4 F10.7 Index from Jan 2010 to Jul 2012 [4].

Data obtained from the RENOIR system for thermospheric vertical winds are shown in Figure 4-5. This vertical wind data plot summarizes all FPI data detected from years of 2009 to 2013 in cardinal mode from which it can be seen that there is a strong dependence of vertical winds on local time and season.

Furthermore, in order to increase our confidence in data usage for further analysis, a cross-comparison between two different measurement modes has been conducted so as to possibly detect any systemic bias in data measurements. Figure 4-6 shows vertical wind data for October 6th, 2010 from both zenith look direction in cardinal mode, and inline direction from common volume mode. A consistency in thermospheric vertical winds between the two modes is clearly seen from this plot. Both modes show similar maximum and minimum values occurring at a same local time.

Hence, this cross comparison of vertical wind data between the cardinal mode and common volume mode indicates that the system bias in measurements should not be significant. Furthermore, this gives confidence that results obtain for vertical winds in this study should not be the result of observational error since these two instrumental modes have very different setups.

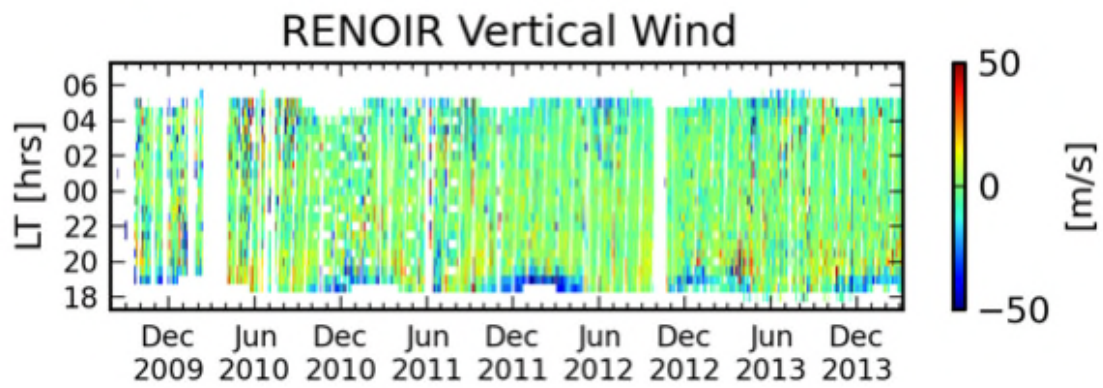


Figure 4-5 Summary of Vertical Wind Data Obtained from RENOIR System [10].

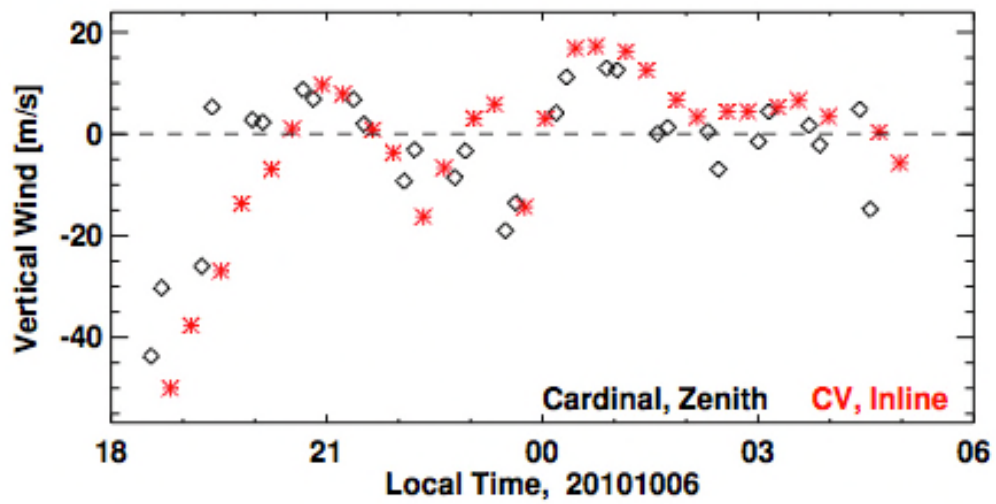


Figure 4-6 Comparison of vertical winds between FPI cardinal mode and FPI common volume mode [10].

Chapter 5

Results and Discussion

In this chapter the results obtained from thermospheric vertical wind analysis are presented. First, seasonal variations of vertical winds are shown, then variations during two storm periods for vertical winds and neutral temperatures are discussed with reference to plot results obtained for different time periods and seasons.

5.1 Seasonal Variation of Vertical Winds

In order to examine the seasonal dependence of vertical winds, we plotted first each month's measurements for the year of 2010, as shown in Figure 5-1. Vertical wind data have been binned according to local time with 30-minute bin size. Error bars in this figure give the standard deviation of the data. From this figure we can see that the standard deviation of vertical winds is larger or comparable with the average value of the winds in most bins, which indicates that vertical winds are averagely small and quite variable. Nevertheless, vertical winds are statistically non-zero at a certain local time showing seasonal dependence as well. For example, vertical winds during hours [19, 21] Local Time (LT) are downward during the months of October, November, and December with values reaching 20 m/s. In contrast, upward vertical winds of 10 m/s are seen for the months of April, May, and June during the same time period [19, 21] LT.

Additionally, vertical winds have been binned in four different seasons during 2010, Figure 5-2. We can see from this figure that before 21 LT winds are mainly upward in spring and summer seasons, turning downward on winter season. Winds experience a transition from downward to upward during the fall season. Moreover, after 4 LT, vertical winds show a consistent downward wind in all seasons while varying in magnitude.

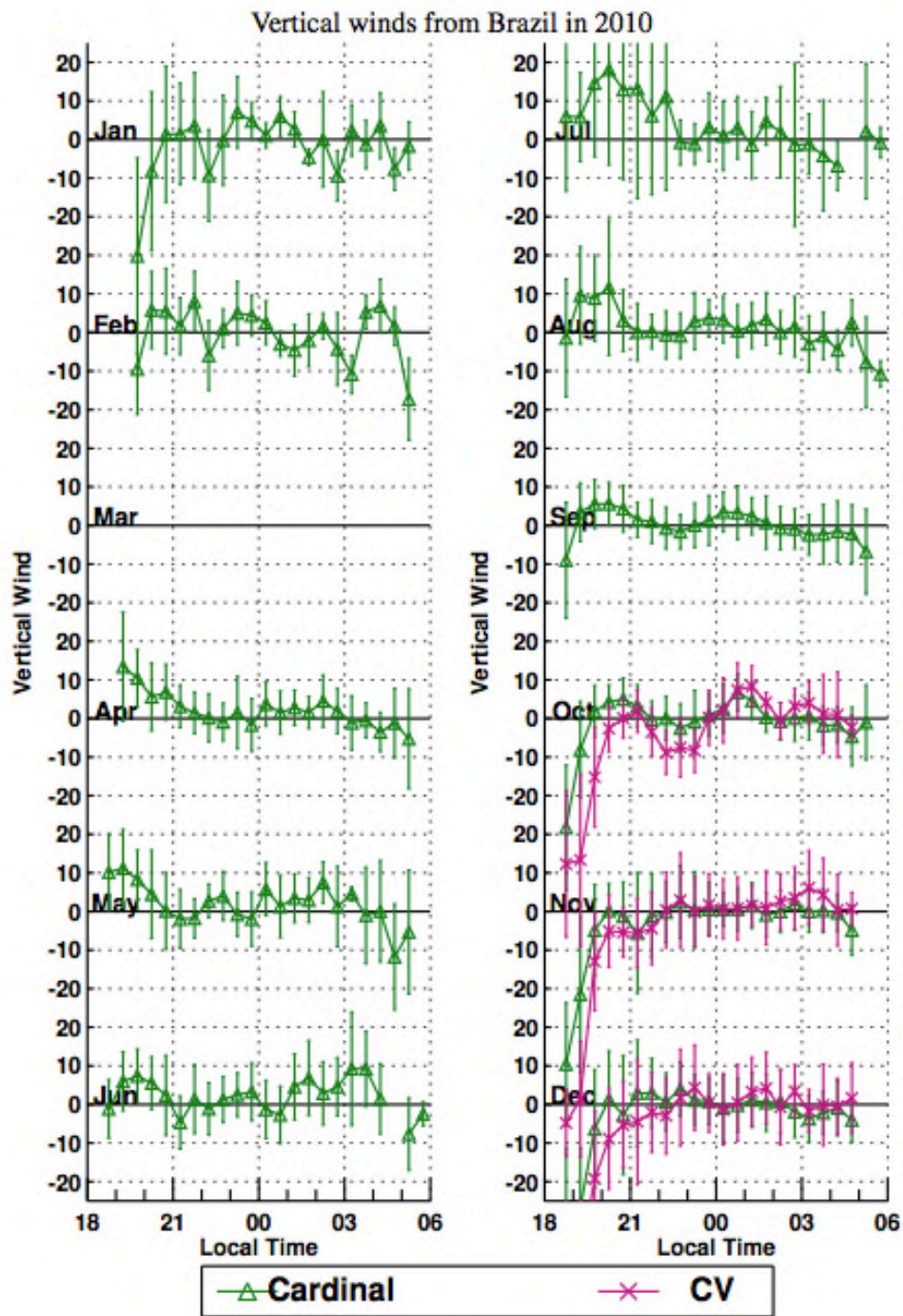


Figure 5-1 Monthly climatologies of vertical winds in 2010. Green triangles represent data from the cardinal mode and magenta crosses from comment volume (CV) mode [10].

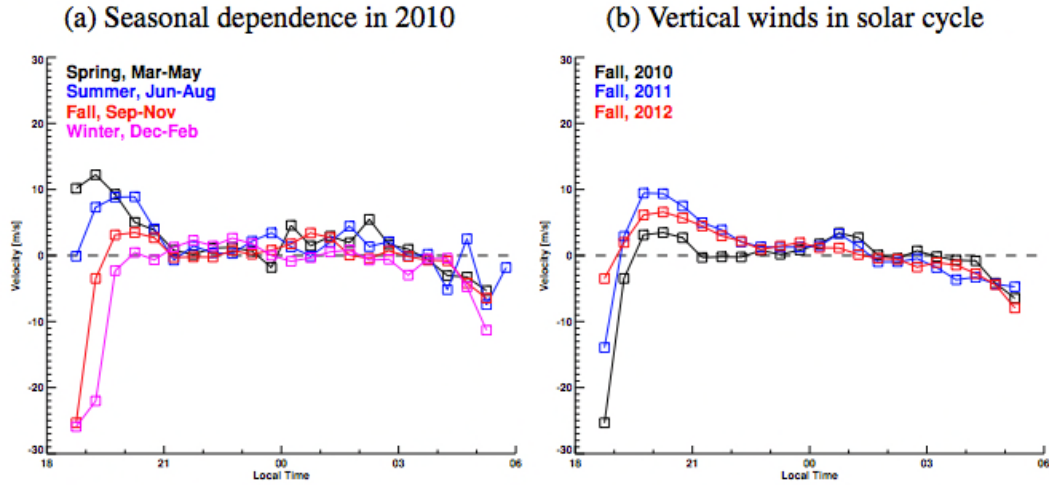


Figure 5-2 (a) Local time variation of average vertical winds in four different seasons for 2010. (b) Local time variation of average vertical neutral winds for the fall season in three for the years of 2010, 2011 and 2012 [10].

The variation of vertical winds with solar cycle is also shown in Figure 5-2 (b). From this right panel of the figure we can see that in Fall 2011, vertical winds reach the largest average upward value of 10 m/s occurring at around 19:30 LT. In Fall 2010, winds shift downward by 7-10 m/s in the period [19,21] LT compared to Fall 2011. A clear seasonal and solar cycle dependence of vertical winds can also be identified. These results show that there are periods where, from a statistical point of view, vertical winds are non-zero. This non-zero result means that there are times where the average value \pm the standard deviation does not include the zero line, which is an indication of average non-zero vertical winds. This interesting non-zero vertical wind result contrasts the typical assumption of zero value vertical winds made in most previous studies since vertical winds are significantly smaller than horizontal winds with wide spread values.

5.2 Vertical Wind Variation During Storms

During storm periods, energy inputs and electrodynamics of the upper atmosphere change significantly causing the neutral winds and temperature to change accordingly. Storm periods are defined according to the geomagnetic activity of the Earth, which can be measured with Kp and Dst indices. The Kp index quantifies on a scale of 0 to 9 the disturbance of the earth's magnetic field. A value of 1 means calm and a value of 5 or more indicates a geomagnetic storm. Similarly, the Dst (disturbance storm time) index estimates the average change of the horizontal component of the earth's magnetic field in negative nano-Tesla (nT) unit values. The size of a geomagnetic storm is classified as moderate ($-50 \text{ nT} > \text{Dst} > -100 \text{ nT}$), intense ($-100 \text{ nT} > \text{Dst} > -250 \text{ nT}$) or super-storm ($\text{Dst} > -250 \text{ nT}$).

For this research study, two storm periods have been selected, the storms of September 17th and 26th, 2011. These two storm periods for the 17th and 26th are shown in Figure 5-3 and Figure 5-4, respectively. Notice from Figure 5-3 that on the day of the storm, the Kp index increased from a very calm storm value of 1 to a more active storm value of 5. Correspondingly, the Dst index marked negative values of less than -50 nT , which was an indication that a geomagnetic storm was actually taking place on the 17th. Similarly, by looking at Figure 5-4, it can be seen that the Kp index went from a calm storm period of value 1 to a stormy period of value 6. Bottom panels on both figures show the corresponding vertical wind and neutral temperature values. Colors represent the intensity of the value in both cases, starting from blue, which is a lower value and scaling up to a red color, which is a higher value. Clearly, we can see that vertical winds on the day of the storm went up by at least 5 m/s while neutral temperatures increased between 100-200 K at a given local time during the storm.

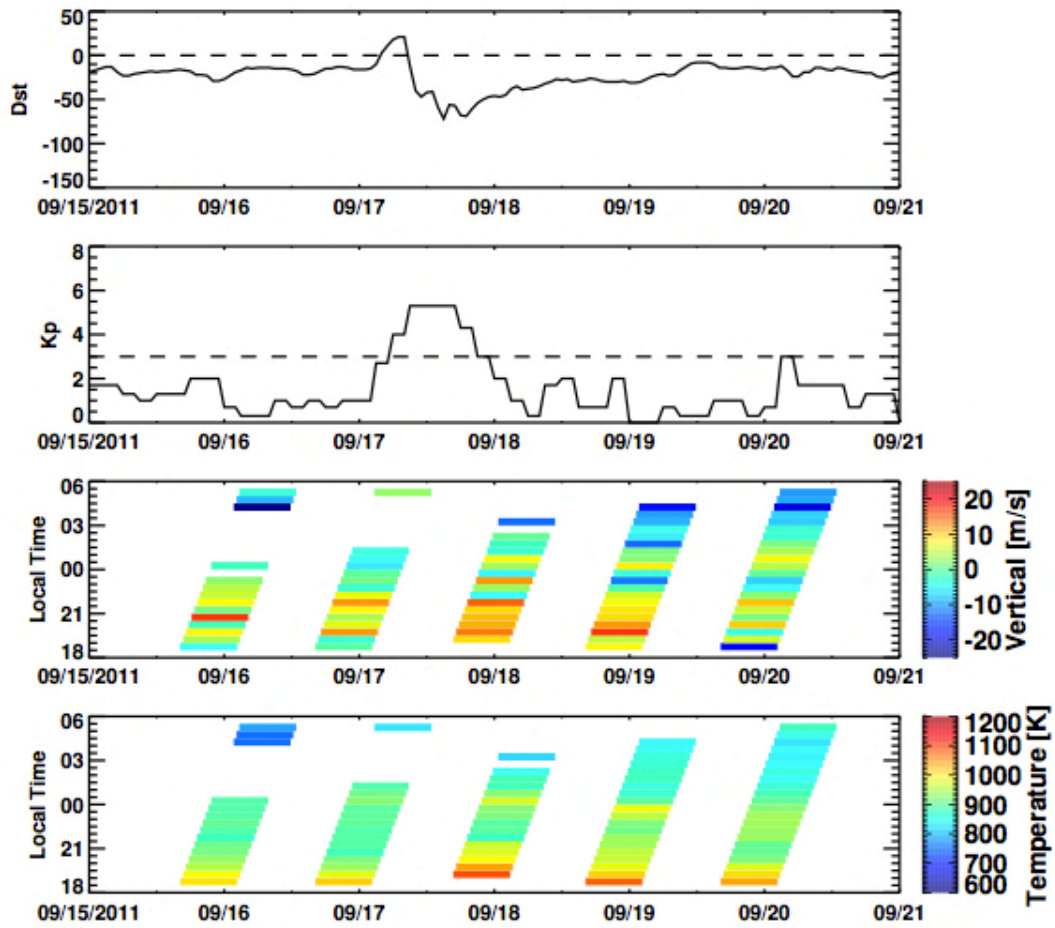


Figure 5-3 Dst, and Kp indices (top two panels), vertical winds and neutral temperature (bottom two panels) during Sept. 17th, 2011 storm [10].

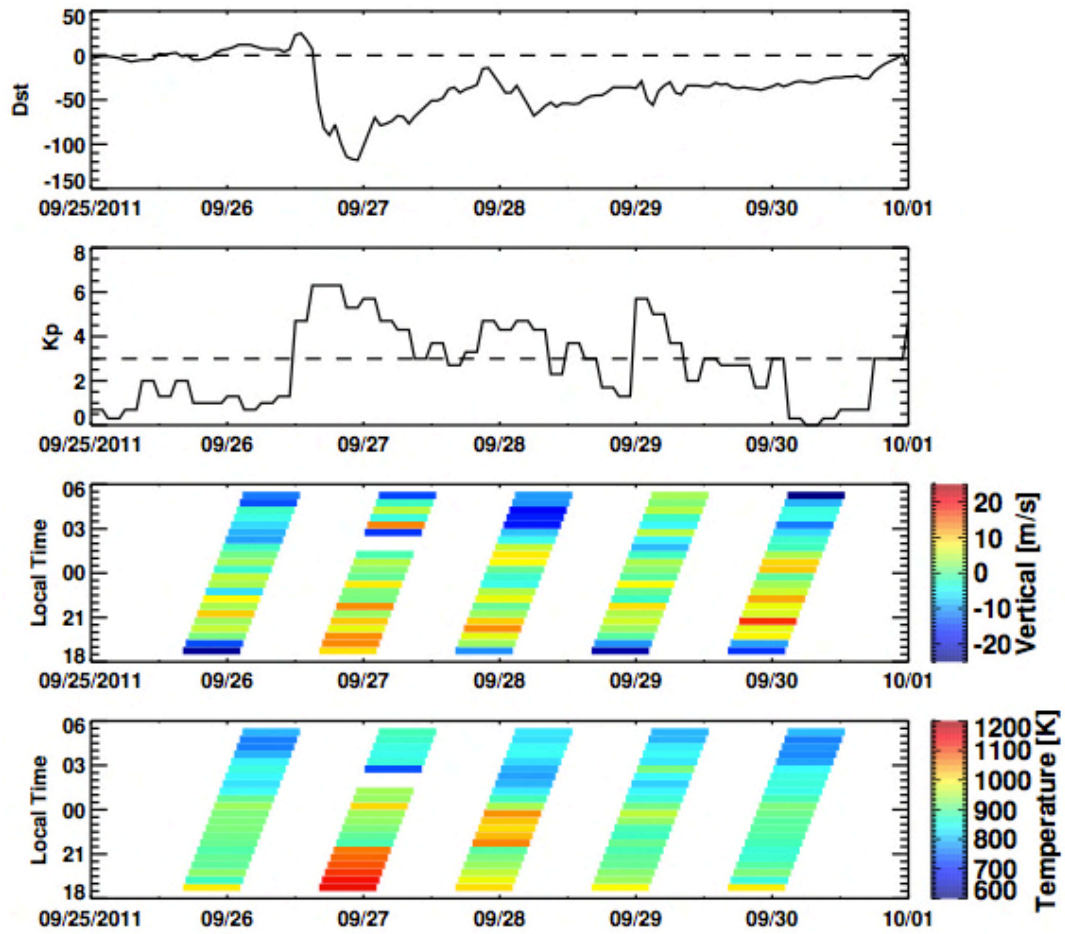


Figure 5-4 Dst, and Kp indices (top two panels), vertical winds and neutral temperature (bottom two panels) during Sept. 26th, 2011 storm [10].

Additionally, FPI measurements of neutral vertical winds and neutral temperatures have been plotted out with respect to universal time for both storm periods. Figure 5-5 shows vertical winds and temperature values for the storm of September 17th, 2011, and Figure 5-6 shows vertical winds and temperatures for storm of September 26th, 2011.

Furthermore, by following Figure 5-5, we can see that thermospheric vertical winds shifted upwards by 5 m/s, on average, the day of the storm, indicated in red color, as compared to wind values from the day previous the storm, indicated in black color. This increase in wind magnitudes is also displayed on top of the curves where average vertical wind values are indicated according to the day of observation. Notice that an average value of 1.59 is marked for the day previous the storm, September 16th, whereas an average value of 5.58 is marked on the day of the storm, September 17th. Thus, an average difference in vertical wind values falls around ~ 5 m/s. Similarly, on the bottom panel of Figure 5-5, we can see that the neutral temperature increased in magnitude by approximately 100 K during the day of the storm as compared to the temperature value from the day previous the storm. Maximum increases in temperature values occurred at the beginning of the night [19,21] local time.

A similar analysis can be done for vertical winds and neutral temperatures for the storm period of September 26th, and shown in Figure 5-6. From this figure we notice an average vertical wind value of -2.93 the day previous the storm, September 25th, meanwhile an average value of 2.52 is indicated the day of the storm, September 26th. Therefore, vertical winds shifted upwards with an average difference value of ~ 5 m/s. Temperature values displayed at the bottom panel of this figure, showed a maximum increased value of 200 K at the beginning of the night, giving a similar trend as that shown in Figure 5-5 during [19,21] LT, but with higher maximum temperature values and bigger differences between storm-day and non-storm day values.

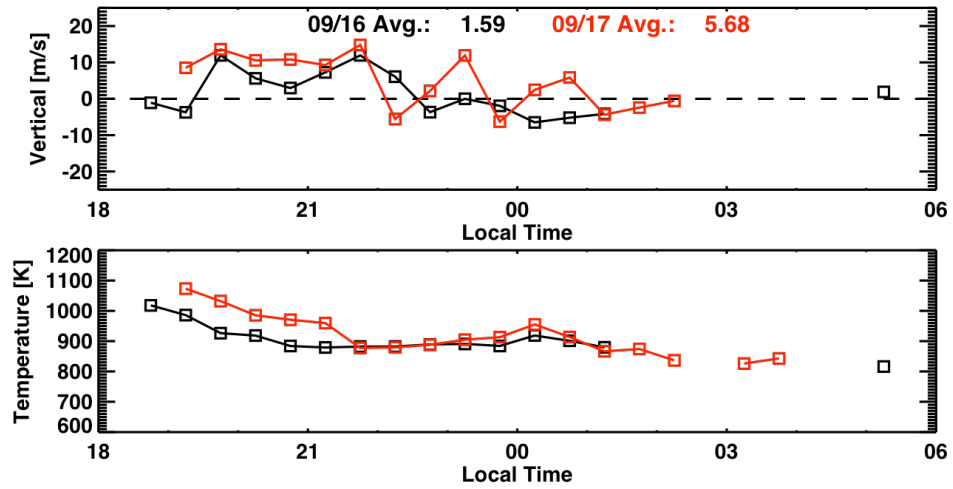


Figure 5-5 FPI measured vertical neutral wind and neutral temperature before (on September 16th) and during (on September 17th) storm period, which are represented by black line and red line, respectively [10].

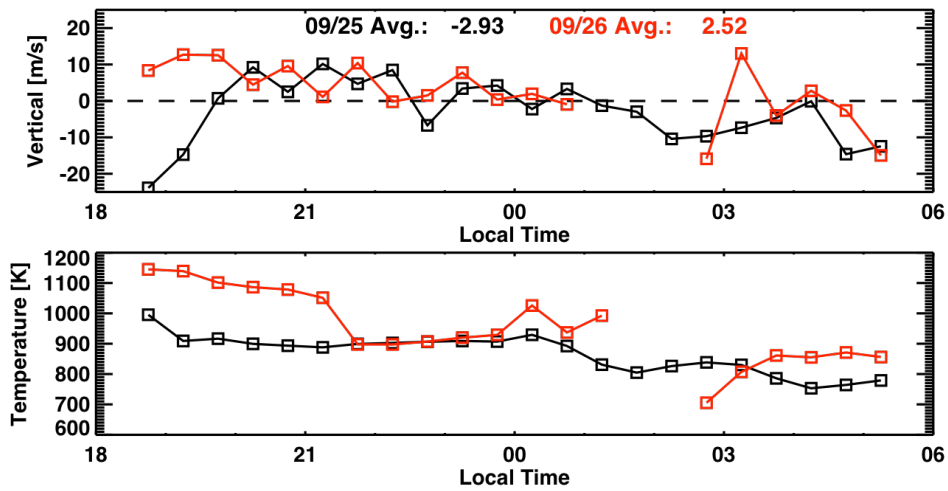


Figure 5-6 FPI measured vertical neutral wind and neutral temperature before (on September 25th) and during (on September 26th) storm period, which are represented by black line and red line, respectively [10].

Chapter 6

Conclusion

6.1 Conclusion

In order to understand upper atmospheric variations, an accurate description of thermospheric winds is essential. As seen from previous analysis (Chapters 4, and 5), vertical winds are small compared to horizontal winds, but even small vertical winds can have a significant effect on the upper atmosphere because of the large vertical density gradients that exist throughout the atmosphere. The bi-static FPI system deployed in Brazil has allowed substantial progress on specifying vertical winds and has provided unprecedented coverage for the study of neutral dynamics of the upper atmosphere.

In this thesis, neutral vertical wind data from Brazil FPI ground-based observations during 2010 to 2013 were used for a climatological study, including the dependencies of vertical winds and neutral temperatures on seasonal and geomagnetic activities. First, a cross comparison study of the data was conducted from two different FPI modes to show that there was no contamination in the measurements and to test the validation of the data. After proving the reliability of the data, measurements were binned according to the local time. Results show statistically non-zero vertical winds at a certain local time and also show a strong seasonal dependence. The variation of vertical wind and neutral temperature during storm time has been studied as well. Vertical winds shifted upwards, on average, by 5 m/s during the two storm periods analyzed, September 17th and 26th, 2011. Similarly, neutral temperatures showed an increase between 100-200 K at the beginning of the night [19,21] LT during the day of the storm as compared to the day previous the storm. All these studies were performed at a low-latitude site with results describing the neutral dynamics of the upper atmosphere at equatorial latitudes.

6.2 Future Work

Besides the two storm periods analyzed, another six storm periods were examined and all of them show a consistent variation of neutral vertical winds and neutral temperature during the geomagnetic storm. Nevertheless, the number of events is still not good enough to formulate a statistical analysis. Therefore, a systematical study should be conducted once more data becomes available during geomagnetic activity. Moreover, a case simulation study of vertical winds and neutral temperatures can be undertaken for periods of high geomagnetic activity.

References

- [1] M. C. Kelley, *The Earth's Ionosphere*. Burlington, MA: Academic Press, 2009.
- [2] Robert Schunk and Andrew Nagy, *Ionospheres*. Cambridge, New York: Cambridge University Press, 2009.
- [3] Daniel J. Fisher, "Three-Dimensional Wind Measurements And Modeling Using A Bi-Static Fabry-Perot Interferometer System In Brazil," Master of Science Thesis, University of Illinois at Urbana-Champaign, 2013.
- [4] J. Makela, J. Meriwether, Daniel J. Fisher, John W. Meriwether, Ricardo A. Buriti, and Amauri F. Medeiros, "Near-continual ground-based nighttime observations of thermospheric neutral winds and temperatures over equatorial Brazil from 2009 to 2012," *Journal of Atmospheric and Solar-Terrestrial Physics* 103 (2013) 94–102. [Online]. Available: <http://www.elsevier.com/locate/jastp>
- [5] M. F. Larsen, and J. Meriwether, "Vertical winds in the thermosphere," *Journal Of Geophysical Research*, Vol. 117, A09319, doi:10.1029/2012JA017843, 2012.
- [6] Gerd W. Pross, *Physics of the Earth's Space Environment*. Springer-Verlag Berlin Heidelberg, 2010.
- [7] King-Hele, D.G., "Average rotational speed of the upper atmosphere from changes in satellite orbits," *Space Res.* 10, 537, 1970.
- [8] Sipler, D.P., and Biondi, M.A., "Equatorial F-region neutral winds from nightglow OI 630.0 nm Doppler shifts," *Geophys. Res. Lett.* 5, 373, 1978.
- [9] A. L. Aruliah, E. M. Griffin, A. D. Aylward, E. A. K. Ford, M. J. Kosch, C. J. Davis, V. S. C. Howells, S. E. Pryse, H. R. Middleton, and J. Jussila, "First direct evidence of mesoscale variability on ion-neutral dynamics using co-located tristatic FPIs and EISCAT radar in Northern Scandinavia," *Annales Geophysicae* (2005) 23: 147–162.

- [10] Yue Deng, Cheng Sheng, Jose De La Garza, Johnathan Makela, Daniel J. Fisher, John Meriwether and Rafael Mesquita, "Analysis of equatorial F-region vertical neutral winds from Brazil FPI observations," *Journal Of Geophysical Research*.
- [11] R. Link and L. Cogger, "A reexamination of the OI 6300- 'A nightglow," *Journal of Geophysical Research*, vol. 93, no. A9, p. 9883, 1988. [Online]. Available: <http://doi.wiley.com/10.1029/JA093iA09p09883>
- [12] Sipler, D. P., M. A. Biondi, and M. E. Zipf (1995), Vertical winds in the midlatitude thermosphere from Fabry-Perot Interferometer measurements, *J. Atmos. Terr. Phys.*, 57, 621–629.
- [13] J. Meriwether, J. Makela, Y. Huang, D. Fisher, R. Buriti, A. Medeiros, and H. Takahashi, "Climatology of the nighttime equatorial thermospheric winds and temperatures over Brazil near solar minimum," *Journal of Geophysical Research*, vol. 116, no. A4, p. A04322, Apr. 2011. [Online]. Available: <http://doi.wiley.com/10.1029/2011JA016477>
- [14] J. Makela, J. Meriwether, Y. Huang, and P. Sherwood, "Simulation and analysis of a multi-order imaging Fabry-Perot interferometer for the study of thermospheric winds and temperatures," *Applied Optics*, vol. 50, no. 22, p. 4403, July 2011. [Online]. Available: <http://www.opticsinfobase.org/abstract.cfm?URI=ao-50-22-4403>
- [15] Aruliah, A. L., and D. Rees, "The trouble with thermospheric vertical winds: Geomagnetic, seasonal and solar cycle dependence at high latitudes," *Journal of Atmospheric and Terrestrial Physics*, 57, 597–609, 1995.

Biographical Information

The physics research assistantship allowed Jose to see more clearly the connection between the theoretical aspect of space physics and the real case studies undertaken by scientists in this area.

Furthermore, research studies seen along the master's degree such as upper atmospheric variations caused by storms caused an interest in him to further the scientific knowledge and experience in a national laboratory or industry.

Presently, Jose's undergraduate preparation in engineering physics combined with his graduate studies in physics provide the tools to enter a field that requires both, theoretical knowledge as well as hands on experience. In particular, the data analysis and simulation skills acquired will open up various opportunities among research and development companies.

Moreover, Jose's graduate education broadened his view of science as a lifelong education. Not only an advanced degree in physics allow him to have a strong mathematical background but also a better understanding of our planet's vulnerabilities to solar storms and its space environment.